Biofabrication

CrossMark

OPEN ACCESS

RECEIVED
22 August 2021

REVISED
23 December 2021

ACCEPTED FOR PUBLICATION
6 January 2022

PUBLISHED
25 January 2022

PAPER

Cancer cell migration on straight, wavy, loop and grid microfibre patterns

Duo Zhang[1], **Yaqi Sheng**[1], **Nicholas Piano**[1], **Theresa Jakuszeit**[2], **Edward Jonathan Cozens**[1], **Lingqing Dong**[1,2,3], **Alexander K Buell**[4], **Andreas Pollet**[5], **Iek Man Lei**[1], **Wenyu Wang**[1], **Eugene Terentjev**[2] **and Yan Yan Shery Huang**[1,*]

[1] Department of Engineering, University of Cambridge, Cambridge, United Kingdom
[2] Cavendish Laboratory, University of Cambridge, Cambridge, United Kingdom
[3] The Affiliated Stomatologic Hospital, School of Medicine, Zhejiang University, Hangzhou, People's Republic of China
[4] Department of Biotechnology and Biomedicine, Technical University of Denmark, Kgs. Lyngby, Denmark
[5] Department of Mechanical Engineering, Eindhoven University of Technology, Eindhoven, The Netherlands
[*] Author to whom any correspondence should be addressed.

E-mail: yysh2@cam.ac.uk

Keywords: breast cancer, cell migration, extracellular matrix, topography, pattern

Supplementary material for this article is available online

Abstract

Cell migration plays an important role in physiological and pathological processes where the fibrillar morphology of extracellular matrices (ECM) could regulate the migration dynamics. To mimic the morphological characteristics of fibrillar matrix structures, low-voltage continuous electrospinning was adapted to construct straight, wavy, looped and gridded fibre patterns made of polystyrene (of fibre diameter ca. 3 μm). Cells were free to explore their different shapes in response to the directly-adhered fibre, as well as to the neighbouring patterns. For all the patterns studied, analysing cellular migration dynamics of MDA-MB-231 (a highly migratory breast cancer cell line) demonstrated two interesting findings: first, although cells dynamically adjust their shapes and migration trajectories in response to different fibrillar environments, their average step speed is minimally affected by the fibre global pattern; secondly, a switch in behaviour was observed when the pattern features approach the upper limit of the cell body's minor axis, reflecting that cells' ability to divert from an existing fibre track is limited by the size along the cell body's minor axis. It is therefore concluded that the upper limit of cell body's minor axis might act as a guide for the design of microfibre patterns for different purposes of cell migration.

1. Introduction

Cell migration refers to the polarisation and locomotion of living cells. It can occur spontaneously and also be driven by a variety of biological, chemical and physical signals [1–3]. Extensive efforts have been made to investigate the effects of physical signals on cell migration, including the role of surface topography and roughness that mimic characteristics of extracellular matrices (ECM) [4–10]. Since the physical architecture and recapitulation of native ECM are complex with multiple global patterns and local topographies, reductionist experimental approaches are valuable in providing mechanistic insights.

Natural ECM derived matrices and synthetic polymers can exist in the form of hydrogels, or other chemically or physically crosslinked polymeric scaffolds [11–19]. These different forms of material interfaces have been used to investigate cell migration. For example, cell-scale collagen bundles aligned on microfluidic devices were used to elicit cell-extracellular matrix interaction in modelling local cancer invasion [20, 21]. Meanwhile, synthetic polymeric materials provide alternative strategy in modelling the physical features of ECM where biochemical factors attributed by naturally derived matrices can be decoupled. For example, micron-scale features (such as grooves, pits or posts) can by fabricated by

stereo-lithography techniques on rigid substrates, to study substrate topography effects on different cellular behaviours including migration [22–26]. Among the different material fabrication strategy, electrospinning could be considered as one of the most facile approaches which produce fibre structures mimicking the physical building blocks of fibrillar ECMs [27–34]. As linear tracks and straight fibre patterns have provided the foundation to recapitulate fibrillar morphology [35–37], it is of interest to evaluate how the features at a higher scale of fibre architecture, such as waviness, loops, and cross-junction grid patterns commonly found in ECM, could influence the cell migration dynamics.

This study adopted a low-voltage continuous electrospinning technique [38] to simplify typical ECM architectures into well-defined and repeatable patterns, and design cell migration assays consisting of individual polystyrene microfibre tracks of straight, wavy, looped or grid patterns. Microfibres (made of polystyrene) were deposited onto substrates (made of polystyrene coated glass slide), with the entire surfaces subjected to plasma treatment, thus cells had the freedom to explore different shapes in response to the well-defined fibril geometries. The combination of such fibre topography with ECM morpho-typical contours could potentially provide new insights into physically-guided cell migration behaviour, compared to established synthetic migration assays such as micro-patterned lanes [39] and channels [40]. Here, this work examines how different global fibre patterns influence the migration dynamics of green fluorescent protein (GFP) transfected MDA-MB-231, a human breast cancer adenocarcinoma cell line characterised by elevated SNX27 (a protein marker of cell mobility and proliferation) expression, and with the highest persistent 2D migration among all breast cancer cell lines [41–44].

2. Results and discussion

2.1. Global fibre pattern determines cell migration direction and cell shape, but not the speed

Disease or age-associated extracellular matrix remodelling often leads to the creation of stiff collagen fibre bundles, which could impart biomechanical cues to cells with their rod-like nature (with several microns in diameter) and nano-scaled surface topography [45–47]. To create synthetic microfibres mimicking the physical attributes of individual stiff ECM fibre bundles, low-voltage continuous electrospinning patterning (LEP), developed in our previous work [38, 48], was used to fabricate polystyrene fibres with required features. Made of polystyrene, such synthetic fibres could provide a chemically stable and robust framework to study cell migration. Figure 1(a) shows the basic fibre printing process. The fibres deposited on polystyrene-coated glass slides have an average diameter of 3 ± 1 μm. In figure 1(b), scanning electron images of single fibres show that the fibre has a circular cross-section and exhibits 'nano-wrinkle' surface features. In figure 1(c), the contact Young modulus of the fibre determined by atomic force microscopy (AFM) nanoindentation was shown to be around 200 MPa, within the range of contact moduli of collagen fibrils (∼0.1–10 GPa) measured by AFM with different buffer solutions [49, 50]. Adjusting the stage collection speed and the application voltage, fibre contours that mimic morphological characteristics of the extracellular matrix, from straight fibres [51–54], to waves and loops [55–60], can be fabricated (figures 1(d)–(g)). To define the wavy fibre features, we fitted sinusoidal functions to the fibre contours. For loop fibres, as the loops were approximated circular (figure 1(e)), the equivalent loop diameters were determined to be between 20 and 40 μm in our study. Finally, for grid patterns, the inter-fibre distances were varied between 0 and 120 μm in orthogonal directions.

Imaging of cell migration experiments were processed with Z-stack projection of cells' GFP fluorescence (SI. figure 1). Results confirmed that each individual fibre had the capacity to guide cell migration (figure 2(a), supplementary movies 1–4 available online at stacks.iop.org/BF/14/024102/mmedia). Aiming at cell on-fibre migration, only cases of single cells on fibril topographies were identified and analysed for the duration. Depending on the fibre pattern, cells adhering to individual fibres, or two parallel fibre tracks, performed guided movement along fibre axes. Cells on a network of orthogonal crossed fibres migrated along either horizontal or vertical directions. Figure 2(b) compares the average step speed (calculated from the distance travelled within 10 min of the imaging interval) for single cell migration on different fibre patterns. The average step speed ranges between 0.2 and 0.5 μm min^{-1} on the four typical global fibre patterns, with no significant difference found between migration on straight aligned fibres and on other complex fibre patterns, or the off-fibre control group. With the finding above, it is suggested that the global fibre pattern affect the direction of cell movement, but not the individual cell step speed. Cell migration speed could be controlled by the intrinsic cell mobility, and the fibre local topographies such as fibre dimension/diameter and surface textures [61–64], which were kept constant in our experiments. Next, analysing single cell morphology in figure 2(c) revealed that as fibre patterns change from open linear to enclosed patterns, the cell aspect ratio increased to a maximum of 0.8 (where aspect ratio = 1 describes a perfect circular shape). Thus, the average shape of a cell is strongly influenced by the fibre pattern, which might have further implications for fibre-guided cell migration. The

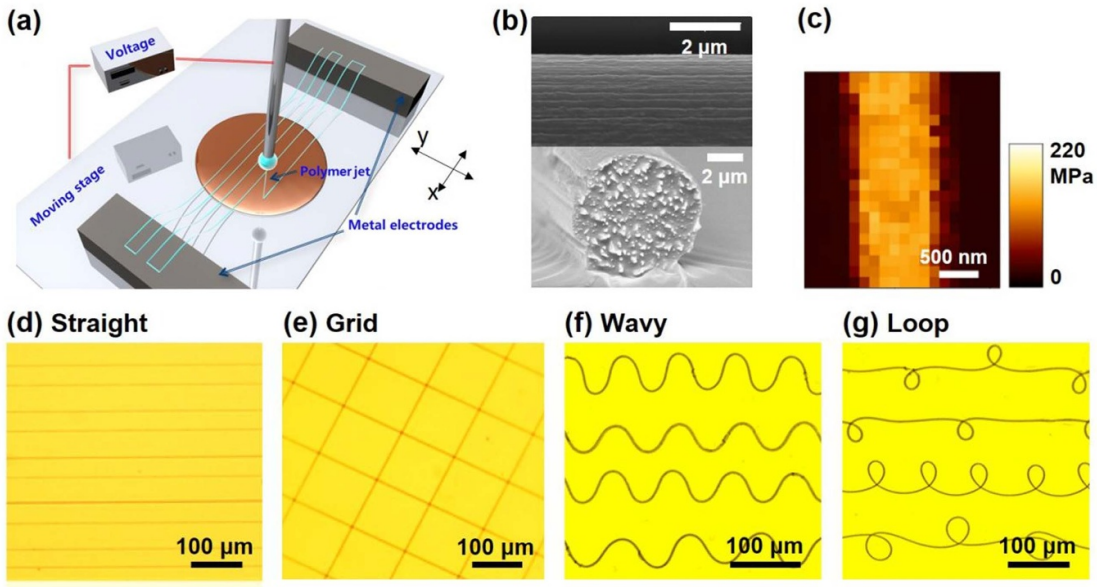

Figure 1. Overviews of the LEP fabricated polystyrene fibres with different global patterns. (a) Schematic figure illustrates the equipment setup of LEP; (b) SEM images showing the nano-wrinkle features and the cross-sectional view of micron-sized fibres; (c) apparent contact stiffness mapping measured by *in situ* AFM indentation on a polystyrene fibre placed on a PDMS substrate of ∼500 kPa to show the contrasting stiffness; (d)–(g) fabricated polystyrene fibres with straight aligned, grid, wavy and loop patterns.

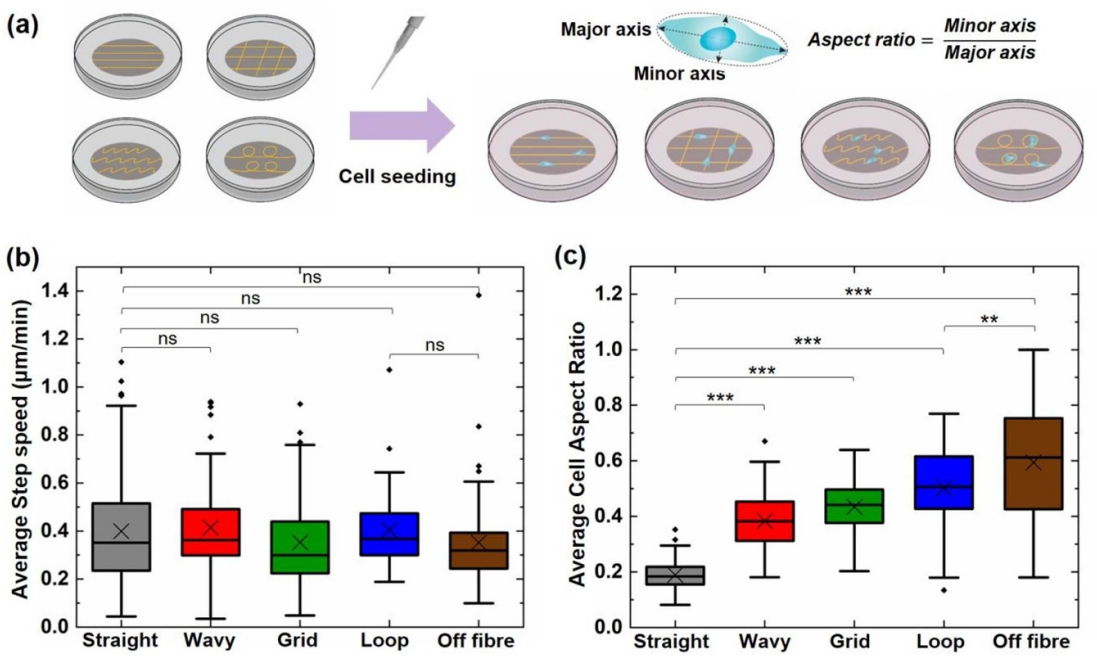

Figure 2. Overview of MDA-MB-231 single cell migration experiments featuring along different fibre patterns. (a) Schematic figure illustrates the cell seeding and migration experiments; (b) cross comparison of single cell step speed when migrating along different fibre patterns, step interval = 10.5 min; (c) cross comparison of single cell aspect ratio when migrating along different fibre patterns. Aspect ratio = minor axis length/major axis length; as each single cell was fitted with an ellipse that optimally approached the cell's boundary. Number of single cells studied: $n = 62$ cells on straight fibres; $n = 90$ cells on wavy fibres; $n = 98$ cells on grid fibres; $n = 52$ cells on loop fibres; $n = 64$ cells on no fibre substrates. All data presented are means ± SDs with superimposed data points. Two sample t-tests were performed, ns denotes no significant difference between groups, $^{**}p < 0.01$, $^{***}p < 0.001$.

following sections analyse cell migration in each of the fibre pattern case in detail, and evaluate how the associated migration behaviour is correlated to the size and shape of the cells.

2.2. Migration dynamics along straight, parallel fibre patterns

For the straight fibres, cells' major axes aligned with the fibre axis, as seen in figure 3(a). Probability maps

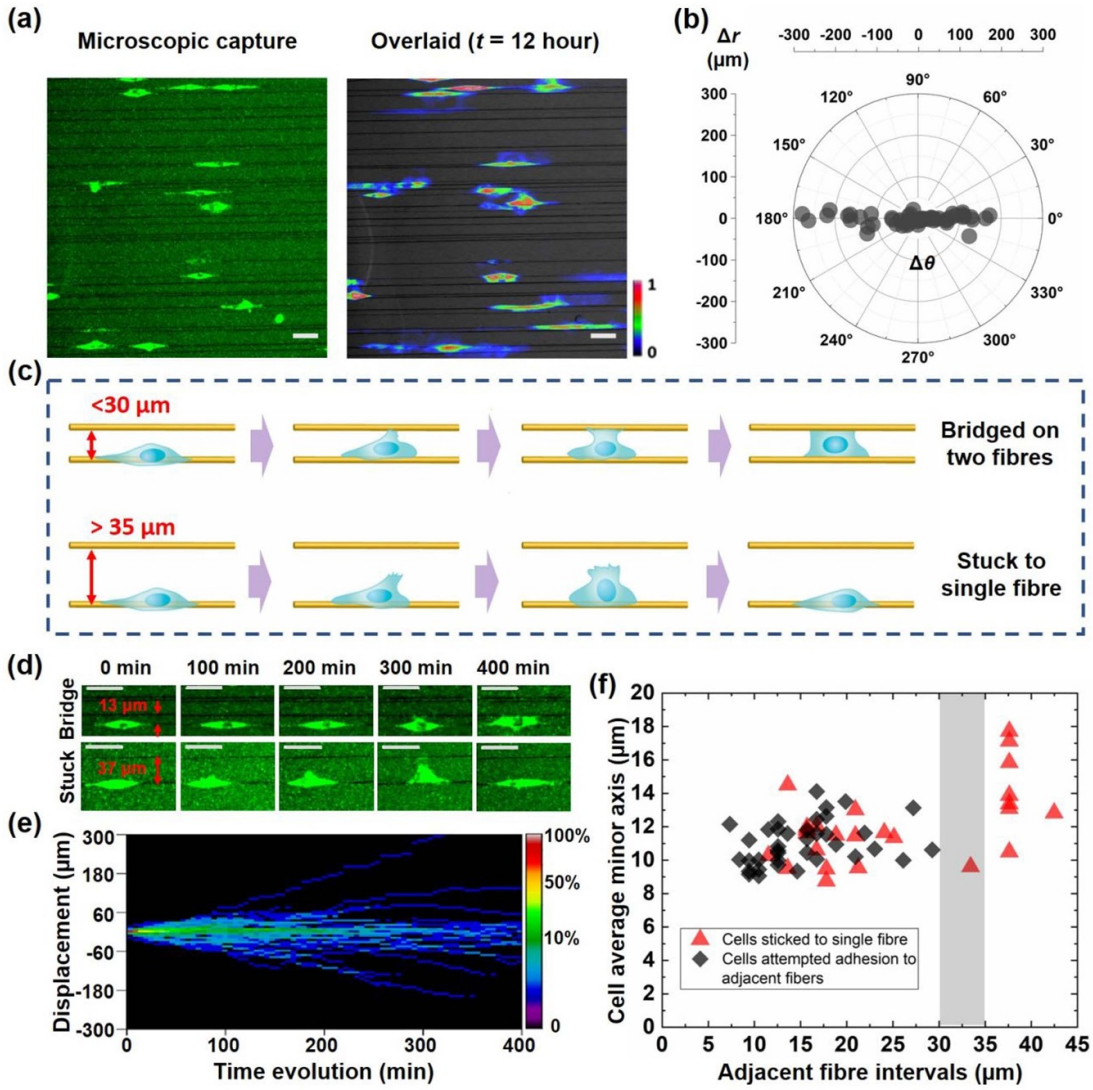

Figure 3. Analysis of MDA-MB-231 single cell migrations along aligned polystyrene microfibres. (a) Fluorescent microscopic image capturing cells migrating on aligned fibres, and the probability map over the 12 h imaging period, scale bar = 50 μm (to note that only the migration dynamics of single, isolated cells were analysed in this study); (b) the polar scattered plot demonstrating cells' ultimate displacements on the aligned fibre patterns over 12 h time periods; (c) schematics showing a single cell would eventually either attempt to hold two parallel fibres (bridge) or stick to the original single fibre, depending on the adjacent fibre interval; (d) set of fluorescent microscopic images showing cases of single cells to either bridge on two fibres, or stuck at single fibre, scale bar = 50 μm; (e) the 400 min accumulated displacement distribution for single cells when they were attached to single fibres; (f) adjacent fibre interval is considered as feature length, and the scattered plot shows the 30–35 μm range fibre interval is a threshold to differentiate single cell behaviours.

are used to illustrate the spatial distribution and activity of the cells over time. Live-cell images were captured at intervals of 10 min and overlapped into a 2D projection image, such that each image pixel numerically represents cell occupancy probability, with a value between 0 and 1. During single cell migration on straight fibres, their major axis was aligned with the fibre axis, and topography guidance provided by the polystyrene microfibres efficiently drove the cells to move along the fibre direction, as shown by figure 3(b). In some cases, a cell could stretch its body sideways and attempt to connect to multiple fibres during migration (bridging between parallel fibres); while in other cases, a cell remained solely on its original fibre track throughout the imaging period (see figures 3(c) and (d), supplementary videos 5 and 6). To evaluate the migration statistics for the single-fibre migration case, cell displacement along the fibre direction was calculated as $\Delta\overrightarrow{x_j}(t) = \overrightarrow{x_j}(t+t_0) - \overrightarrow{x_j}(t_0)$, where $\overrightarrow{x_j}(t+t_0)$ denotes the position vector (in 1D system only motion in one axis is considered) of the jth cell at time t, and t_0 represents the corresponding original starting time. The displacement vs. time plot for all the cells tracked for the straight fibre patterns, is shown in figure 3(e). The ensemble-averaged displacement trajectories of cells were in symmetry with respect to the zero horizontal line, supporting the equal likeliness for the cells to migrate towards either end of the fibre.

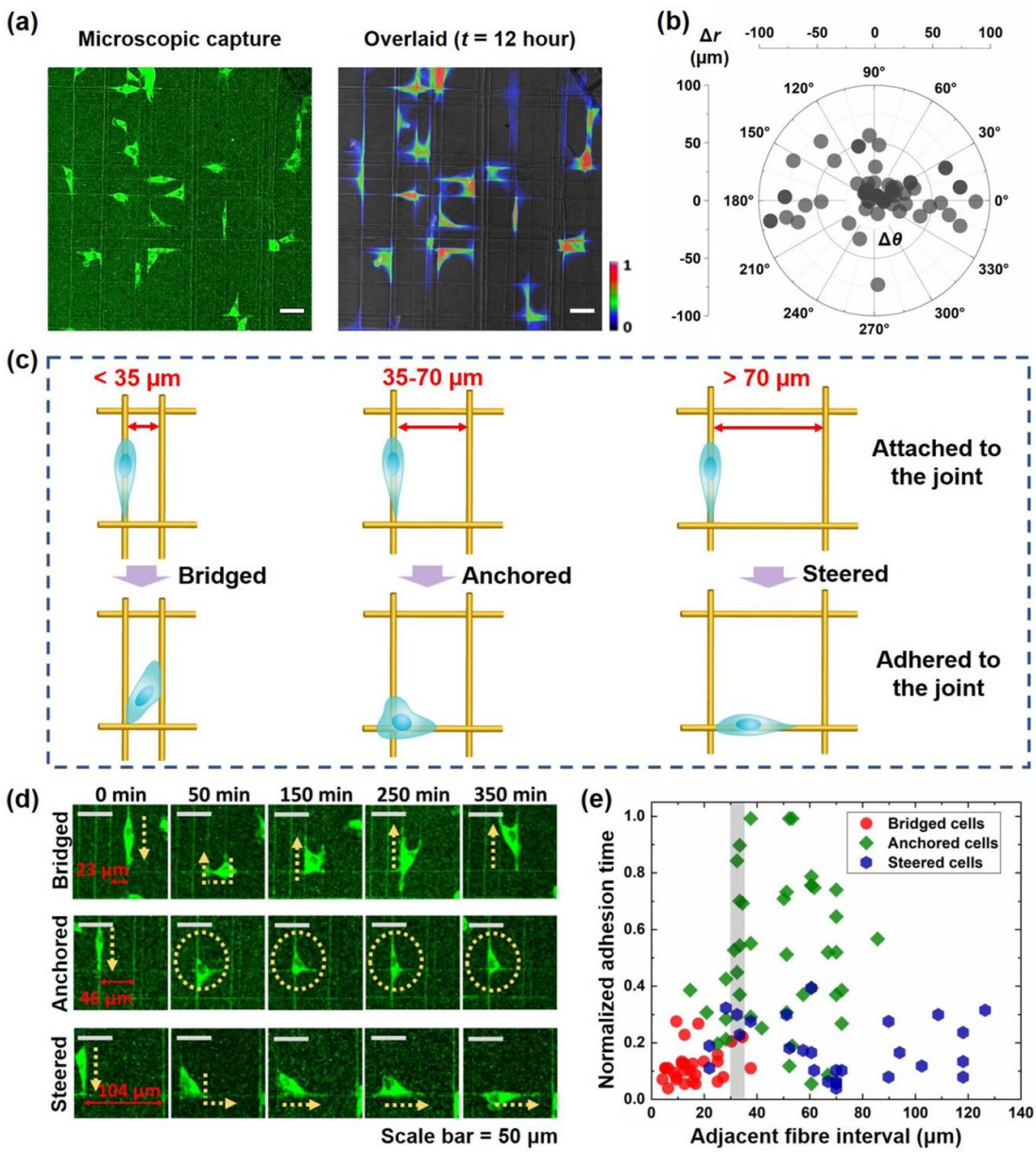

Figure 4. Analysis of MDA-MB-231 single cell migration along grid polystyrene microfibre patterns. (a) Fluorescent microscopic image capturing cells migrating on fibre grids, and the probability map over the 12 h imaging period, scale bar = 50 μm; (b) the polar scattered plot demonstrating cells' ultimate displacements on the grid fibre patterns over 12 h time evolution; (c) schematics demonstrating three typical scenarios of single cell movements when migrating towards the grid fibre joints; (d) set of fluorescent microscopic images showing cases of single cells to respectively bridge, anchor or steer at the fibre joint, scale bar = 50 μm; (e) the scattered plot demonstrating the correlation between adjacent fibre intervals and cells' normalised adhesion. The threshold fibre interval (feature length) range is around 30–35 μm.

Further categorisation of single-fibre and parallel fibre migration behaviours in figure 3(f) suggests that the spacing between parallel fibres (i.e. fibre interval) is a determining parameter. When the inter-fibre distance was smaller than 30 μm, there was no preferred choice for the cell behaviour (either remain on a single fibre or bridging to neighbouring fibres). However, when the fibre interval was increased to over 35 μm, cell bridging was no longer observed, and cells remained on their original linear fibre. Figure 3(f) shows that cell minor axis length all had values below ca. 18 μm. Thus, it is suggested that the distance of adjacent fibres is the characteristic dimension of the parallel fibres, which determines whether a cell is able to be diverted from its current fibre migration path. The length of the cell minor axis could be used as a measure of their ability to stretch their body orthogonal to the fibre direction, and reach an adjacent fibre for migration.

2.3. Migration dynamics along grid patterns

Looking over the 12 h live-cell imaging period, an interesting observation is that most cells are restricted to their local grid/boxed meshes, which is shown in the fluorescent microscopic image as well as the probability map in figure 4(a). The possible reason

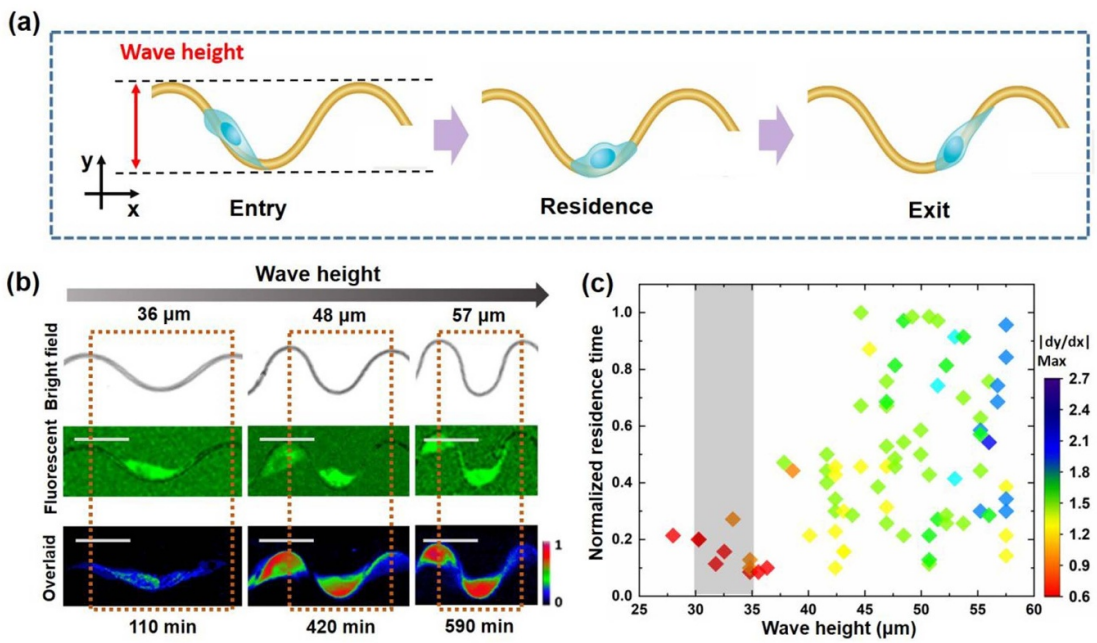

Figure 5. Analysis of MDA-MB-231 single cell migrations along wavy polystyrene microfibre patterns. (a) Schematic diagrams illustrating different stages of a single cell migrating across a wavy curve; (b) cell behaviours differ as wave height increases, demonstrated in microscopic images in bright field, green fluorescent channel and time-accumulated probability maps, scale bar = 50 μm; (c) scattered distribution shows the wavy features (wave height and $|dy/dx|_{\max}$) influence cells' normalised residence. The 30–35 μm range in 'wave height' acts as a threshold that differentiates cell residence. 'Wave height' is defined as the difference between the elevations of a crest and a neighbouring trough (also twice the amplitude of the fitted sine wave).

is that within the time of measurement, cells would inevitably come across orthogonal fibre joints, which appear as a local protuberant landscape to the cells. When a cell comes across an orthogonal fibre joint, its protrusions are able to sense orthogonal fibres, and the cell reacts accordingly to adapt to different fibril topography. The ultimate displacement of cells during the entire experimental session was calculated and displays in figure 4(b). Compared to cells on straight aligned fibres, this distribution shows that grid joints provide an extra degree of freedom to cell migration.

Next, the single cell migration was studied. Figure 4(c) illustrates three types of single cell behaviour that were observed when interacting with orthogonal fibre junctions: (i) bridged at joints, where a single cell would bridge to the adjacent parallel fibre track and then continue migrating along the two parallel tracks simultaneously; (ii) anchored at joints, where a single cell would remain anchored at these joints; and (iii) steered at joints, where a single cell would be redirected along one of the orthogonal fibre tracks. Figure 4(d) further demonstrates typical cases of the above scenarios in sequential fluorescent microscopic images, indicating general time durations (additional detailed examples are shown in supplementary videos 7–9). To characterise the migration behaviour, 'cell adhesion time' is defined as the total time that a cell is adhered at a fibre junction, from the initial point the cell body first touches the joint, until the moment that all parts of the cell body have lost contact with the joint. As shown in figure 4(e), when the normalisation of this parameter (cell adhesion time/total imaging time) is plotted against the adjacent fibre distance, the different cell behaviour falls into distinct categories. When the adjacent fibre distance is less than 30–35 μm, multiple cell behaviours was observed, though cell bridging dominates at narrow fibre spacing. As adjacent fibre distance becomes greater than ~30–35 μm, cell bridging can no longer take place. For adjacent fibre distance above 70 μm, cells would then be redirected at these junctions to an orthogonal fibre track for continued migration.

2.4. Migration dynamics along wavy and loop fibre patterns

ECM fibrils often have curly geometries [58, 60], with features similar to cell sizes, and such geometries can be categorised into two major groups: wavy and closed-loop patterns. For wavy fibre patterns, the curve can be described by a sinusoidal function of $y = A \cdot \sin(2\pi x/\lambda)$, with A being the amplitude and λ the wavelength. Focusing on single cell-fibre interaction, the migration along a wavy fibre segment is illustrated in figure 5(a), where cells were observed to maintain contact with the fibre throughout the migration. A cell entering a wavy curve is defined to be the moment when the cell body firstly touch a trough/crest (where $dy/dx = 0$); and a cell leaving the wavy curve is defined as the moment when the cell body has fully passed over the curve trough/crest. Cell residence time represents the total

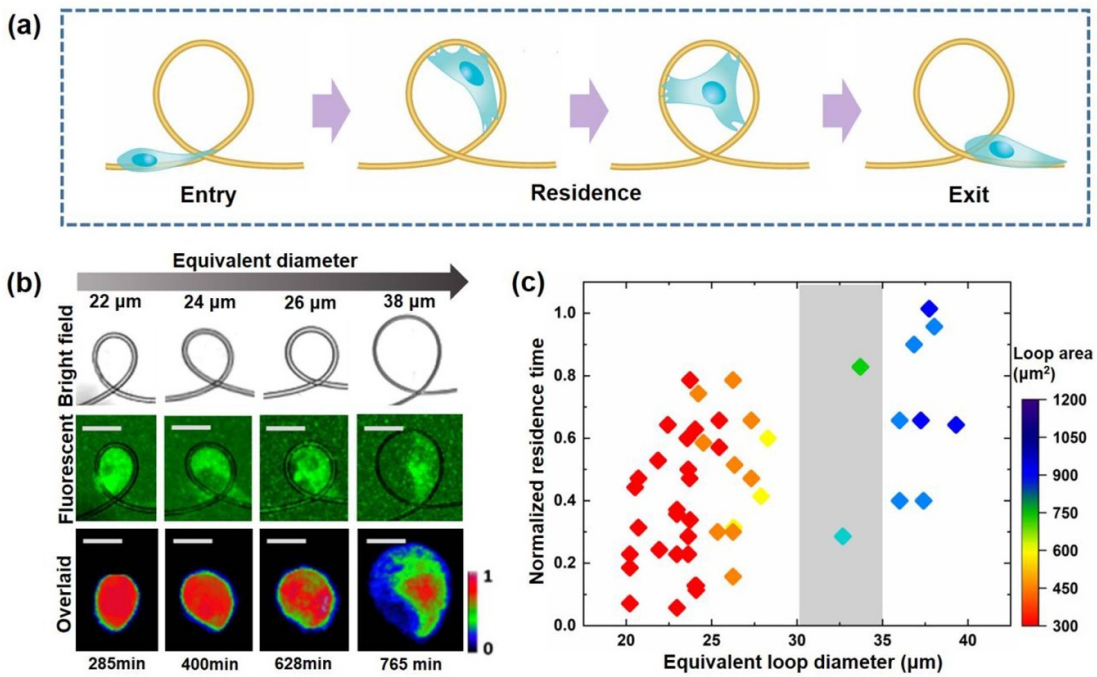

Figure 6. Analysis of MDA-MB-231 single cell migrations within loop polystyrene microfibre patterns. (a) Schematic diagrams illustrating different stages of a single cell migrating across a fibre loop; (b) cell behaviours differ as loop size (equivalent diameter) increases, demonstrated in microscopic images in bright field, green fluorescent channel and time-accumulated probability maps, scale bar = 50 μm; (c) scattered distribution between the normalised cell residence and the fibre loop size. Equivalent loop diameter is considered as the feature length; the 30–35 μm range in 'equivalent diameter' is considered as the threshold feature length that indicate different cell residence.

time that a cell spent passing across a wavy fibre curve. Figure 5(b) displays three typical cases of microscopic images, showing different sizes of wavy fibre curves in bright field, and correspondent cell shapes in fluorescent channel (additional detailed examples are shown in supplementary videos 10–12). Cell residence times are also displayed alongside the probability maps, highlighting that as the waveform amplitude increased, coupled with increased curliness, cell residence seemed to be prolonged.

To quantify the curliness of wavy fibres, 'curve steepness' was characterised as the maximum derivative ($|dy/dx|_{\max}$) for each of the sinusoidal segment. Thus figure 5(c) shows the effect of wavy fibre contour, characterised by wave height ($2 \times A$) and steepness ($|dy/dx|_{\max}$) on cell residence. When the wave height increased beyond ~30–35 μm, along with the increased curve steepness, the normalised cell residence times increased rapidly. In some cases, the 'cell residence time/total time duration' ratio approached 1, indicating that these cells were trapped inside the curve throughout the entire imaging period. It should be noted that as the curve steepness is increased, there are still cases of cells having lower residence time. This is because cells were observed to enter fibre curves at different times during the imaging session, thus low residence values were recorded for cells entering towards the end of the imaging session.

The close-loop patterns demonstrated an efficient 'cell trapping' ability when the loop diameters are close to the cell size. Figure 6(a) shows stages of cell transiting through a loop pattern, where the cell residence time is defined as the total time elapsed for a cell staying inside a loop. Figure 6(b) displays example microscopic images, showing different sizes of fibre loops in bright field, and correspondent cells in fluorescent channel (additional detailed examples are shown in supplementary videos 13–15). For small loops with diameters of around 20 μm, cells tended to occupy the entire loop space, and having some of its cell body extending beyond the loop. For medium size loops with diameters of approximately 25–30 μm, cells would still be able to accommodate the majority of the loop space. In contrast, for large loops, with diameters greater than 35 μm, cells could only adhere to a portion of the loop boundary, and would accordingly only occupy smaller portions of the loop. Figure 6(c) presents the correlation between the normalized cell residence and the loop diameter. As the loop diameter increases from 20 to 35 μm, the cell residence gradually shifted up to around 70% of the time.

3. Discussion and conclusion

For all the global microfibre patterns studied in this work, MDA-MB-231 cells were able to execute fibre-guided migrations, while adapting their morphologies to fit in local topographies as well as global fibre patterns. As shown in figure 7(a), our results point to the threshold feature length for aligned, wavy, loop

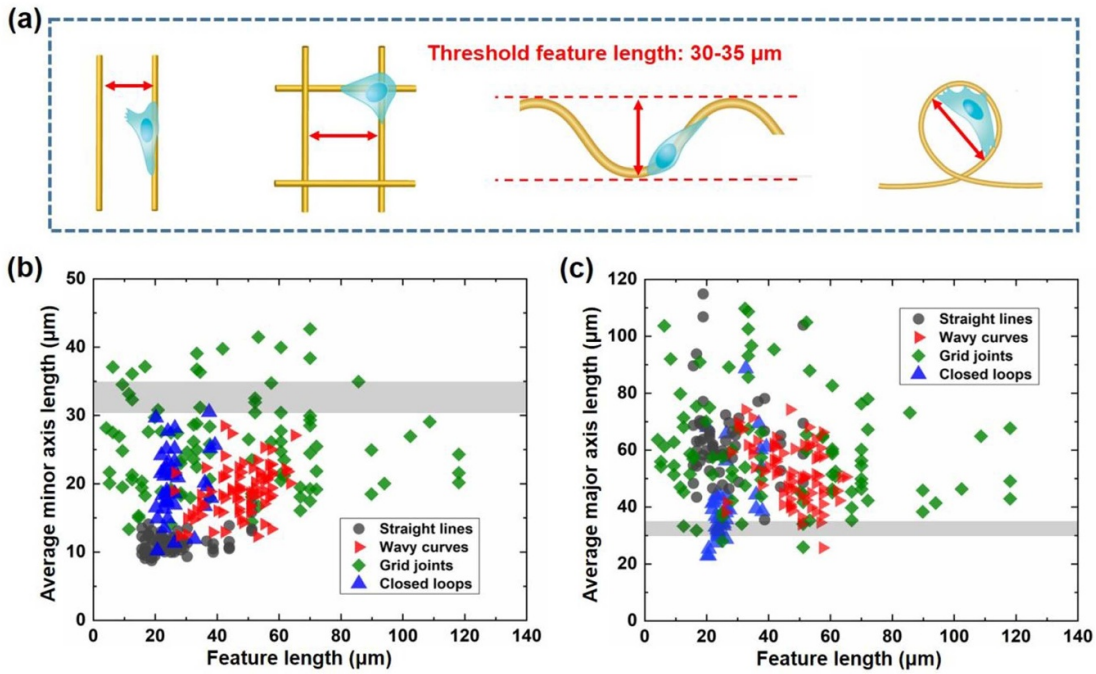

Figure 7. Feature length reflects the capability for MDA-MB-231 cells to stretch and adapt to the fibril environment. (a) Schematic diagrams showing that at different fibre patterns, the threshold feature length are all in the range of 30–35 μm; (b), (c) scattered plots of the average minor and major axis length for all single cells in different fibre patterns, revealing that the upper limit of the cells' minor axis length, and the lower limit of cells' major axis length, along with marking for the threshold feature length of 30–35 μm.

and grid fibre patterns and are all at the range of 30–35 μm for which the MDA-MB-231 cells would switch their migration behaviour. It is intuitive to reason that this critical pattern feature size would be related to intrinsic cell body shape features.

Our live cell imaging results indicated highly dynamical nature of visible cellular protrusions, which were formed to probe surrounding topography, subsequently guide the displacement of the cell body (SI. figures 2 and 3). Imaging data showed that visible cell protrusion lengths could go far beyond the range of 30–35 μm, which were generated and afflicted to the fibre structures (e.g. SI. figure 3). In addition, our prior work showed that long protrusions could break from the main cell body to release the cell to travel away from the protrusion breakage fragments [65]. The above experimental observations suggest that the upper lengths of protrusions themselves is not a factor for crossing migration paths.

Therefore, this work examined the minor axis length and the major axis length of the cell bodies in all experiments, as plotted in figures 7(b) and (c). It is shown that the upper limit of the cell body's minor axis length, and the lower limit of cell body's major axis length, are both in the range of 30–35 μm. The 'coincidence' of these two values led us to postulate the following: A cell can have different movements to accommodate fibre patterns during migration; different fibre patterns will determine the motion as well as the shape of the cell body. However, chances for a cell to alter its pre-existing fibre migration path depend on its body's ability to stretch sideways and reach the adjacent fibre, and thus could be determined by the upper limit of its minor axis. For MDA-MB-231 cells which attached to an existing fibre, the maximum distance that they can reach and form stabilised adhesion on another fibre, over the preference of existing fibre alone, is in the range of 30–35 μm. Although experiments in this work were performed on fibres patterned on a planar (2D) substrate, it is postulated that the similar outcomes would be manifested in a 3D fibrous network. A plane is defined by two lines that intersect or are parallel; hence, the fibres on a 2D geometry represent a subsect that reflects the upper limit for track diversion in a 3D fibrous network.

To conclude, this work reports the systematic analysis of MDA-MB-231 cell migration dynamics along polystyrene fibres fabricated using low-voltage continuous electrospinning. The fabrication of fibre networks with straight, curly and grid patterns provided geometric environments to study how cells sense and interact with complex morphologies. Cells were able to dynamically adapt their shapes in response to the adhered fibre, as well as to the neighbouring patterns; such adaptation reflects their ability to traverse between fibre tracks. Key dynamical and morphological features such as the variation of cell step speed and minor axis were identified for understanding cell migration in fibril matrices, as well as designing future ECM-mimic fibril models for cell migration studies.

4. Experimental sections

4.1. Coating glass slides

The glass slides (diameter: 22 mm) used for depositing polystyrene fibres were coated using a spin-coater (Model WS-650MZ-23MPPB). For each glass slide, 70 μl 2 wt% polystyrene (Mw $\sim$ 280.000 kDA, Sigma-Aldrich) in toluene (anhydrous 99.8%, Sigma-Aldrich) solution was initially added at the centre. The glass slides were spun for 10 s at 500 rpm, followed by 50 s at 1000 rpm. Coated glass slides were then dried at reduced pressure for 24 h, following which they could be stored at room temperature for several weeks.

4.2. Fibre printing

Low-voltage continuous electrospinning patterning technology (LEP) was used to print polystyrene fibres on polystyrene coated glass slides. The setup consists of a supporting aluminium plate and silicon plate under the glass slide, aluminium initiators at both sides of the polystyrene coated glass slide, and a power source and syringe pump. Coated glass slides were placed between two aluminium initiators on a supporting aluminium plate for fibre deposition. The printing stage was heated up to 33.5 °C to ensure continuous jetting during printing. After the stage had settled at this temperature, a 1 ml syringe with a 25 G needle was filled with a 25 wt% polystyrene in dimethylformamide (DMF) (Sigma-Aldrich) solution for fibre printing, and a flow rate of 160 μl h^{-1} was set. During the printing process, the stage was initially lifted slowly until it had reached the needle of the syringe. The positive and negative poles of the voltage output device were connected to the needle and the stage respectively. Polystyrene fibres were directly written onto the coated substrate under an applied voltage ranging from 0.3 to 0.7 kV. The global fibre pattern shape can also be affected by the voltage level applied. A voltage of 0.5 kV marked the transition between straight and curly fibres for 25 wt% polystyrene/DMF mixture. To fabricate straight aligned fibre patterns, the working voltage was set at 0.3 kV. To fabricate all curly fibres, working voltage was further increased to 0.5–0.7 k V. To fabricate grid fibre patterns, a first layer of straight aligned fibres were initially deposited, followed by rotation of the substrate by 90 degrees to deposit a second layer of aligned fibres.

4.3. Atomic force microscopy (AFM) characterisation

In situ AFM nano-indentation was performed using a Nanowizard AFM (JPK Instruments, Germany). Measurements were taken in distilled water at room temperatures. The preparation procedure involved fixing the sample onto a piece of mica using araldite and inserting it into a liquid cell. The samples were immersed in distilled water for over 10 min prior to measurement. A Hertizian model [66] was employed to extrapolate the apparent contact stiffness and a silicon tip (NSC36, Mikromasch, frequency 100–200 kHz) was used for the measurement. For the *in situ* AFM, measurements were performed on polystyrene fibres deposited on a thin spin-coated PDMS (polymethyldioxane, modulus $\sim$500 kPa) film. This allows to show contrasting stiffness values between the fibre and the background in the stiffness mapping.

4.4. Fibre pre-treatment for cell migration

A series of pre-treatments were followed to make fibres on polystyrene-coated glass slides ready for cell adhesion and migration experiments. First, silicon rubber compound (RS 555–588) was used to fix the fibre-printed glass slide on a petri dish (diameter: 35 mm). This petri dish had a hole cut in the centre, using a machine in advance, and the fibre-printed glass slide was fixed right above this hole. After fixing, plasma treatment was applied with a flow rate of 25 m^3 s^{-1} for 45 s to provide polystyrene fibres with hydrophilic surface. Afterwards, the petri dish was sterilised under UV light for 30 min, following which the fibre-printed glass slide were immersed in 4 ml PBS for 24 h in the hood. Finally, PBS was replaced with 3 ml cell culture medium and the fibres were immersed for 48 h in a standard cell incubator; the immersing culture medium was changed every 24 h.

4.5. Cell culture

GFP-labeled MDA-MB-231 human breast cancer cells were cultured in Dulbecco's modified Eagle's medium (DMEM, Invitrogen) supplemented with 1% L-glutamine (Invitrogen), 10% foetal bovine serum (FBS), 1% penicillin and 100 μg ml^{-1} streptomycin (Sigma Aldrich). To reduce fluorescence quenching during culture, aluminium foil was used to wrap the culture flasks. The culture medium was changed every 2 d, and cell passage was performed when 80% of the flask was covered by cells.

4.6. Live cell imaging

Live cell imaging was performed on 35 mm petri dishes with fibre-deposited, PS-coated glass slides. 30 000–40 000 cells were suspended in 2 ml cell culture medium, resulting in a cell density of 1.5–2 $\times$ 10^4 cells ml^{-1} to be deposited into the petri-dish for the single cell migration imaging. Higher cell seeding densities would potentially make more cells attach to fibre paths and eventually affect the motions of their neighbouring cells, while we tried to stay with a 'single-track' concept. An estimated period of 2–3 h was given in advance before the imaging initiated, in order for most of the cells to attach to fibres; and their migration dynamics were captured every 10.5 min in the time-lapse microscopy for a continuous 12 h time period. Z-stack imaging of the cells' GFP fluorescence were applied, since a single plane of confocal imaging does not provide sufficient imaging quality

for cell shape segmentation. The cell Z-stack imaging and time-lapse experiments were performed using an environmentally controlled chamber joined to a Leica confocal microscope (Leica TCS SP5). The heater was set to 37 °C to heat up the stage top incubator, and sterilised water and CO_2 were used to provide a suitable moisture and pH inside the box-type incubator. During imaging, excitation was set at 480 nm and detection was set at around 500 nm to observe the GFP signal, and the bright field signal was also collected. For cell migrations along straight aligned fibres, experiments were conducted with $N = 7$ replicates; 4–16 single cells were observed in each experimental replica, resulting a total of 62 single cells analysed. For cell migrations along grid fibres, experiments were conducted with $N = 9$ replicates; 3–23 singles cells were observed in each experimental replica, resulting in a total of 98 single cells analysed. For cell migrations along wavy fibres, experiments were conducted with $N = 4$ replicates; 15–34 single cells were observed in each experimental replica, resulting in a total of 90 single cells analysed. For cell migrations along loop fibres, experiments were conducted with $N = 4$ replicates; 7–23 single cells were observed in each experimental replica, resulting in a total of 52 single cells analysed. For the control groups of cell migrations along no-fibre substrates, experiments were conducted with $N = 3$ replicates; 5–50 single cells were observed in each experimental replica, resulting in a total of 64 single cells analysed.

4.7. Post-processing and statistical analysis

For the image analysis, an image analysis program written in-house was used to pre-process the live-cell images and to create a database to classify the microenvironment-based interaction automatically. The program incorporates a code to analyse the z-stack images, and a number of open-source applications, including ImageJ plug-ins and CellProfiler pipelines, in an adapted procedure following our prior study [67]. The GFP intensity of the z-stack imaging acquired during the time-lapse experiments was projected into one x–y plane at each time point; thus the projected cell area, that is the 2D projection of the 3D cell shape, was obtained at each time point. The Manual Tracking plugin of ImageJ, applied to the projected GFP sequence, was used to track the position of the cancer cell nuclei over time. Single cells that were long-lasting in the acquisition view, kept moving along single a fibre and were distanced from other cells, were generally chosen for tracking. Home-written Matlab codes were used for most analysis of cell migration. The image analysis software CellProfiler was applied to perform the segmentation of the cancer cell projected area and to extract the cell shape features in the different microenvironments at each time point. Cells were labelled with unique ID, and cell shapes were recognised and segmented from the microscopic images. In terms of single cell migration studies, only single cells with good shape recognitions were collected; cells with defective shape recognitions were excluded. The cancer cell coordinates were corrected to take into account the fluctuations of the microscope stage that occurred during experiments.

Data availability statement

The data that support the findings of this study are available upon reasonable request from the authors.

Acknowledgments

This work was supported by the European Research Council (ERC-StG 758865). D Z, Y S and W W were recipients of the Chinese Scholar Councils (CSC) Studentship. I M L acknowledges the financial support from the W D Armstrong Trust and the Macao Postgraduate Scholarship Fund. AKB thanks the Novo Nordisk Foundation for funding (NNFSA170028392). We would also like to thank our previous group members Dr Xia Li and Dr Zhaoying Li for initial protocol developments.

Conflict of interest

The authors declare that they have no known competing financial interests or personal relationships that could have appeared to influence the work reported in this paper.

ORCID iDs

Duo Zhang https://orcid.org/0000-0002-7737-9229
Yaqi Sheng https://orcid.org/0000-0002-3545-6601
Theresa Jakuszeit https://orcid.org/0000-0003-3848-7486
Alexander K Buell https://orcid.org/0000-0003-1161-3622
Andreas Pollet https://orcid.org/0000-0002-9571-2902
Iek Man Lei https://orcid.org/0000-0002-6337-1592
Wenyu Wang https://orcid.org/0000-0001-6580-8236
Eugene Terentjev https://orcid.org/0000-0003-3517-6578
Yan Yan Shery Huang https://orcid.org/0000-0003-2619-730X

References

[1] Trepat X, Chen Z and Jacobson K 2012 Cell migration *Compr. Physiol.* **2** 2369–92
[2] Balzer E M, Tong Z, Paul C D, Hung W, Stroka K M, Boggs A E, Martin S S and Konstantopoulos K 2012 Physical confinement alters tumor cell adhesion and migration phenotypes *FASEB J.* **26** 4045–56

[3] Charras G and Sahai E 2014 Physical influences of the extracellular environment on cell migration *Nat. Rev. Mol. Cell Biol.* **15** 813–24
[4] Van Horssen R and Ten Hagen T L M 2011 Crossing barriers: The new dimension of 2D cell migration assays *J. Cell. Physiol.* **226** 288–90
[5] Werner M, Petersen A, Kurniawan N A and Bouten C V 2019 Cell-perceived substrate curvature dynamically coordinates the direction, speed, and persistence of stromal cell migration *Adv. Biosyst.* **3** 1900080
[6] Ashby W J and Zijlstra A 2012 Established and novel methods of interrogating two-dimensional cell migration *Integr. Biol.* **4** 1338
[7] Song K H, Park S J, Kim D S and Doh J 2015 Sinusoidal wavy surfaces for curvature-guided migration of T lymphocytes *Biomaterials* **51** 151–60
[8] Huergo M A C *et al* 2014 Dynamic scaling analysis of two-dimensional cell colony fronts in a gel medium: a biological system approaching a quenched Kardar-Parisi-Zhang universality *Phys. Rev.* E **90** 022706
[9] Löber J, Ziebert F and Aranson I S 2014 Modeling crawling cell movement on soft engineered substrates *Soft Matter* **10** 1365–73
[10] Li Z *et al* 2018 Solution fibre spinning technique for the fabrication of tuneable decellularised matrix-laden fibres and fibrous micromembranes *Acta Biomater.* **78** 111–22
[11] Weaver V M, Petersen O W, Wang F, Larabell C A, Briand P, Damsky C and Bissell M J 1997 Reversion of the malignant phenotype of human breast cells in three- dimensional culture and *in vivo* by integrin blocking antibodies *J. Cell Biol.* **137** 231–45
[12] Gordon V D *et al* 2003 Measuring the mechanical stress induced by an expanding multicellular tumor system: a case study *Exp. Cell Res.* **289** 58–66
[13] Bernstein J J, Goldberg W J and Laws E R 1994 Migration of fresh human malignant astrocytoma cells into hydrated gel wafers *in vitro Brain Tumor Invasiveness* **18** 63–73
[14] Jung S, Ackerley C, Ivanchuk S, Mondal S, Becker L E and Rutka J T 2001 Tracking the invasiveness of human astrocytoma cells by using green fluorescent protein in an organotypical brain slice model *J. Neurosurg.* **94** 80–89
[15] Rao S S, DeJesus J, Short A R, Otero J J, Sarkar A and Winter J O 2013 Glioblastoma behaviors in three-dimensional collagen-hyaluronan composite hydrogels *ACS Appl. Mater. Interfaces* **5** 9276–84
[16] Ananthanarayanan B, Kim Y and Kumar S 2011 Elucidating the mechanobiology of malignant brain tumors using a brain matrix-mimetic hyaluronic acid hydrogel platform *Biomaterials* **32** 7913–23
[17] Yang Y-L, Sun C, Wilhelm M E, Fox L J, Zhu J and Kaufman L J 2011 Influence of chondroitin sulfate and hyaluronic acid on structure, mechanical properties, and glioma invasion of collagen I gels *Biomaterials* **32** 7932–40
[18] Coquerel B, Poyer F, Torossian F, Dulong V, Bellon G, Dubus I, Reber A and Vannier J-P 2009 Elastin-derived peptides: matrikines critical for glioblastoma cell aggressiveness in a 3D system *Glia* **57** 1716–26
[19] David L, Dulong V, Coquerel B, Le Cerf D, Cazin L, Lamacz M and Vannier J-P 2008 Collagens, stromal cell-derived factor-1α and basic fibroblast growth factor increase cancer cell invasiveness in a hyaluronan hydrogel *Cell Prolif* **41** 348–64
[20] Zanotelli M R *et al* 2019 Energetic costs regulated by cell mechanics and confinement are predictive of migration path during decision-making *Nat. Commun.* **10** 4185
[21] Gong X, Kulwatno J and Mills K L 2020 Rapid fabrication of collagen bundles mimicking tumor-associated collagen architectures *Acta Biomater.* **108** 128–41
[22] Kim D-H, Seo C-H, Han K, Kwon K W, Levchenko A and Suh K-Y 2009 Guided cell migration on microtextured substrates with variable local density and anisotropy *Adv. Funct. Mater.* **19** 1579–86
[23] Bettinger C, Langer R and Borenstein J 2009 Engineering substrate topography at the micro- and nanoscale to control cell function *Angew. Chem., Int. Ed. Engl.* **48** 5406–15
[24] Lovmand J *et al* 2009 The use of combinatorial topographical libraries for the screening of enhanced osteogenic expression and mineralization *Biomaterials* **30** 2015–22
[25] Brunette D M and Chehroudi B 1999 The effects of the surface topography of micromachined titanium substrata on cell behavior *in vitro* and *in vivo J. Biomech. Eng.* **121** 49–57
[26] Oakley C and Brunette D M 1993 The sequence of alignment of microtubules, focal contacts and actin filaments in fibroblasts spreading on smooth and grooved titanium substrata *J. Cell Sci.* **106** 343–54
[27] Tsang M W *et al* 2003 Human epidermal growth factor enhances healing of diabetic foot ulcers *Diabetes Care* **26** 1856–61
[28] Mustoe T 2004 Understanding chronic wounds: a unifying hypothesis on their pathogenesis and implications for therapy *Am. J. Surg.* **187** S65–70
[29] Boulter E *et al* 2013 CD98hc (SLC3A2) regulation of skin homeostasis wanes with age *J. Exp. Med.* **210** 173–90
[30] Schaue D and McBride W H 2015 Opportunities and challenges of radiotherapy for treating cancer *Nat. Rev. Clin. Oncol.* **12** 527–40
[31] Wyld L, Audisio R A and Poston G J 2015 The evolution of cancer surgery and future perspectives *Nat. Rev. Clin. Oncol.* **12** 115–24
[32] Wang Y, Gutierrez-Herrera E, Ortega-Martinez A, Anderson R R and Franco W 2016 UV fluorescence excitation imaging of healing of wounds in skin: evaluation of wound closure in organ culture model *Lasers Surg. Med.* **48** 678–85
[33] Gao Q *et al* 2020 3D printed multi-scale scaffolds with ultrafine fibers for providing excellent biocompatibility *Mater. Sci. Eng.* C **107** 110269
[34] Xie C, Gao Q, Wang P, Shao L, Yuan H, Fu J, Chen W and He Y 2019 Structure-induced cell growth by 3D printing of heterogeneous scaffolds with ultrafine fibers *Mater. Des.* **181** 108092
[35] Xue N, Li X, Bertulli C, Li Z, Patharagulpong A, Sadok A and Huang Y Y S 2014 Rapid patterning of 1-D collagenous topography as an ECM protein fibril platform for image cytometry *PLoS One* **9** e93590
[36] Gill E L, Li X, Birch M A and Huang Y Y S 2018 Multi-length scale bioprinting towards simulating microenvironmental cues *Bio-Des. Manuf.* **1** 77–88
[37] Doyle A D, Wang F W, Matsumoto K and Yamada K M 2009 One-dimensional topography underlies three-dimensional fibrillar cell migration *J. Cell Biol.* **184** 481–90
[38] Li X *et al* 2016 Low-voltage continuous electrospinning patterning *ACS Appl. Mater. Interfaces* **8** 32120–31
[39] Sniadecki N J, Desai R A, Ruiz S A and Chen C S 2006 Nanotechnology for cell-substrate interactions *Ann. Biomed. Eng.* **34** 59–74
[40] Faure-André G *et al* 2008 Regulation of dendritic cell migration by CD74, the MHC class II-associated invariant chain *Science* **322** 1705–10
[41] Zhang J *et al* 2019 Deletion of sorting nexin 27 suppresses proliferation in highly aggressive breast cancer MDA-MB-231 cells *in vitro* and *in vivo BMC Cancer* **19** 555
[42] Betapudi V, Licate L S and Egelhoff T T 2006 Distinct roles of nonmuscle myosin II isoforms in the regulation of MDA-MB-231 breast cancer cell spreading and migration *Cancer Res.* **66** 4725–33
[43] Denoyelle C, Hong L, Vannier J-P, Soria J and Soria C 2003 New insights into the actions of bisphosphonate zoledronic acid in breast cancer cells by dual RhoA-dependent and -independent effects *Br. J. Cancer* **88** 1631–40
[44] Maiuri P *et al* 2012 The first world cell race *Curr. Biol.* **22** 673–5
[45] Lu P, Weaver V M and Werb Z 2012 The extracellular matrix: a dynamic niche in cancer progression *J. Cell Biol.* **196** 395–406

[46] Frantz C, Stewart K M and Weaver V M 2010 The extracellular matrix at a glance *J. Cell. Sci.* **123** 4195–200
[47] Bonnans C, Chou J and Werb Z 2014 Remodelling the extracellular matrix in development and disease *Nat. Rev. Mol. Cell Biol.* **15** 786–801
[48] Li Z, Li X and Huang Y Y S 2021 Low-voltage continuous electrospinning: a versatile protocol for patterning nano- and micro-scaled fibers for cell interface *Methods Mol. Biol.* **2147** 125–35
[49] Wenger M P E, Bozec L, Horton M A and Mesquidaz P 2007 Mechanical properties of collagen fibrils *Biophys. J.* **93** 1255–63
[50] Wen C Y *et al* 2012 Collagen fibril stiffening in osteoarthritic cartilage of human beings revealed by atomic force microscopy *Osteoarthr. Cartil.* **20** 916–22
[51] Provenzano P P, Inman D R, Eliceiri K W, Trier S M and Keely P J 2008 Contact guidance mediated three-dimensional cell migration is regulated by Rho/ROCK-dependent matrix reorganization *Biophys. J.* **95** 5374–84
[52] Taufalele P V, VanderBurgh J A, Muñoz A, Zanotelli M R and Reinhart-King C A 2019 Fiber alignment drives changes in architectural and mechanical features in collagen matrices *PLoS One* **14** e0216537
[53] Kular J K, Basu S and Sharma R I 2014 The extracellular matrix: structure, composition, age-related differences, tools for analysis and applications for tissue engineering *J. Tissue Eng.* **5** 204173141455711
[54] Wang W Y, Davidson C D, Lin D and Baker B M 2019 Actomyosin contractility-dependent matrix stretch and recoil induces rapid cell migration *Nat. Commun.* **10** 1186
[55] Provenzano P P, Eliceiri K W, Campbell J M, Inman D R, White J G and Keely P J 2006 Collagen reorganization at the tumor-stromal interface facilitates local invasion *BMC Med.* **4** 38
[56] Crabb R A B, Chau E P, Decoteau D M and Hubel A 2006 Microstructural characteristics of extracellular matrix produced by stromal fibroblasts *Ann. Biomed. Eng.* **34** 1615–27
[57] Wang L, Johnson J A, Zhang Q and Beahm E K 2013 Combining decellularized human adipose tissue extracellular matrix and adipose-derived stem cells for adipose tissue engineering *Acta Biomater.* **9** 8921–31
[58] Lansky Z, Mutsafi Y, Houben L, Ilani T, Armony G, Wolf S G and Fass D 2019 3D mapping of native extracellular matrix reveals cellular responses to the microenvironment *J. Struct. Biol.* X **1** 100002
[59] Padhi A and Nain A S 2020 ECM in differentiation: a review of matrix structure, composition and mechanical properties *Ann. Biomed. Eng.* **48** 1071–89
[60] Winkler J, Abisoye-Ogunniyan A, Metcalf K J and Werb Z 2020 Concepts of extracellular matrix remodelling in tumour progression and metastasis *Nat. Commun.* **11** 5120
[61] Berry C C, Campbell G, Spadiccino A, Robertson M and Curtis A S G 2004 The influence of microscale topography on fibroblast attachment and motility *Biomaterials* **25** 5781–8
[62] Schwartz M A and Horwitz A R 2006 Integrating adhesion, protrusion, and contraction during cell migration *Cell* **125** 1223–5
[63] Ge L, Yang L, Bron R, Burgess J K and Van Rijn P 2020 Topography-mediated fibroblast cell migration is influenced by direction, wavelength, and amplitude *ACS Appl. Bio Mater.* **3** 2104–16
[64] Van Helvert S, Storm C and Friedl P 2018 Mechanoreciprocity in cell migration *Nat. Cell Biol.* **20** 8–20
[65] Xue N, Bertulli C, Sadok A and Huang Y Y S 2014 Dynamics of filopodium-like protrusion and endothelial cellular motility on onedimensional extracellular matrix fibrils *Interface Focus* **4** 20130060
[66] Oliver W C and Pharr G M 2004 Measurement of hardness and elastic modulus by instrumented indentation: advances in understanding and refinements to methodology *J. Mater. Res.* **19** 3–20
[67] Bertulli C, Gerigk M, Piano N, Liu Y, Zhang D, Müller T, Knowles T J and Huang Y Y S 2018 Image-assisted microvessel-on-a-chip platform for studying cancer cell transendothelial migration dynamics *Sci. Rep.* **8** 12480